ADVANCED MATERIALS INTERFACES
Open Access
www.advmatinterfaces.de

Determining the Electronic Structure and Thermoelectric Properties of $MoS_2/MoSe_2$ Type-I Heterojunction by DFT and the Landauer Approach

Oscar A. López-Galán, Israel Perez, John Nogan, and Manuel Ramos*

The electronic structure and thermoelectric properties of MoX_2 (X = S, Se) Van der Waals heterojunctions are reported, with the intention of motivating the design of electronic devices using such materials. Calculations indicate the proposed heterojunctions are thermodynamically stable and present a band gap reduction from 1.8 eV to 0.8 eV. The latter effect is highly related to interactions between metallic d-character orbitals and chalcogen p-character orbitals. The theoretical approach allows to predict a transition from semiconducting to semi-metallic behavior. The band alignment indicates a type-I heterojunction and band offsets of 0.2 eV. Transport properties show clear n-type nature and a high Seebeck coefficient at 300 K, along with conductivity values (σ/τ) in the order of 10^{20}. Lastly, using the Landauer approach and ballistic transport, the proposed heterojunctions can be modeled as a channel material for a typical one-gate transistor configuration predicting subthreshold values of ≈60 mV dec^{-1} and field–effect mobilities of ≈160 cm^{-2} V^{-1} s^{-1}.

1. Introduction

Molybdenum disulfide (MoS_2) and layered transition metal dichalcogenides (TMD) are promising candidates for developing next-generation electronic, spintronic, and optoelectronic devices. This is because of several advantages as semiconductors, like a transition from indirect to direct band gap (in MoS_2 occurs ≈1.1 eV to ≈1.9 eV),[1–3] excellent mechanical properties,[4] an on–off ratio of about 10^8,[5] electron mobilities between 30 cm^{-2} V^{-1} s^{-1} and 200 cm^{-2} V^{-1} s^{-1},[6] and a layered nature that allows new functionality by merging atomically thin parts of distinct materials. In addition, Van der Waals heterojunctions made of TMD are the subject of intense research[7–11] as an attractive way to tune the electronic performance of devices. From this, exceptional properties can be found, including carrier tunneling,[12] metallic states in Moiré patterns,[13,14] and Van der Waals–Janus type heterojunctions.[15]

In this regard, Roy et al. experimentally achieved Van der Waals heterojunctions between MoS_2/WSe_2 by mechanical exfoliation of the layers.[16] They created a dual-gate device architecture that works based on the quantum tunneling of carriers, similar to other reported Van der Waals heterojunctions like MoS_2/WS_2,[17] PbI_2/MoS_2,[18] and hexagonal boron nitride (h-BN)/MoS_2.[19] Ji et al. studied a multilayer $MoS_2/MoSe_2$ heterostructure whereby Density Functional Theory (DFT) under different conditions of lattice constraint.[20] The results predicted an enhancement in electron mobility about 1.5 times higher than in pure MoS_2 due to band structure change after heterojunction formation. In the former research, authors also considered

O. A. López-Galán
Institute of Nanotechnology (INT)
Karlsruhe Institute of Technology (KIT)
Hermann-von-Helmholtz-Platz 1
76344 Eggenstein-Leopoldshafen, Germany
E-mail: oscar.galan@partner.kit.edu; oscar.lopez@uacj.mx

O. A. López-Galán
Institute for Applied Materials – Materials Science and Engineering (IAM-WK)
Karlsruhe Institute of Technology (KIT)
Engelbert-Arnold-Str. 4, D-76131 Karlsruhe, Germany

The ORCID identification number(s) for the author(s) of this article can be found under https://doi.org/10.1002/admi.202202339.

DOI: 10.1002/admi.202202339

I. Perez
Consejo Nacional de Ciencia y Tecnología-Departamento de Física y Matemáticas
Instituto de Ingeniería y Tecnología
Universidad Autónoma de Ciudad Juárez
Avenida del Charro #450, Ciudad Juárez, Chihuahua 32310, Mexico

J. Nogan
Center for Integrated Nanotechnologies
Sandia National Laboratories
1101 Eubank Bldg. SE, Albuquerque, NM 87110, USA

M. Ramos
Departamento de Física y Matemáticas
Instituto de Ingeniería y Tecnología
Universidad Autónoma de Ciudad Juárez
Avenida del Charro #450 N, Ciudad Juárez, Chihuahua 32310, Mexico

different coupling conditions, which ultimately show a potential route for band gap engineering. Similarly, Zheng et al. proved by DFT calculations that charge transfer between layers depends on temperature and valence band maximum location on MoS_2/WS_2 heterojunctions.[21] Recently, Bellus et al. investigated the band alignment in MoS_2/ReS_2 heterojunctions using DFT calculations.[22] Their analysis reveals a type-I band alignment. Furthermore, the orbital projection indicates that both the valence band maximum (VBM) and the conduction band minimum (CBM) locate at the ReS_2 layer. This results in an incoherent charge transfer due to the lattice mismatch in the MoS_2/ReS_2 heterostructure. Terrones et al. showed that interlayer alignment and stacking order influenced the properties of Van der Waals heterojunctions, predicting indirect to direct band gap transition even at multilayer arrangements.[23] Similar reports indicate that lattice constraint, interlayer alignment, and lattice mismatch play a critical role in determining both structural and electronic properties of such materials.[24–26] For this, we argue that it is essential further investigation of the different coupling conditions and arrangements between MoS_2 and $MoSe_2$, thus, being able to predict their electronic structure, resembling the conditions taking place experimentally.

This work aims to determine the change in the electronic structure with coupling conditions of Van der Waals heterojunction between MoS_2 and $MoSe_2$ under a dispersion corrected DFT (DFT-D2) scheme. With this, we can determine if the proposed arrangement is feasible to implement as a channel material in, e.g., a field–effect transistor or solar cells. We predicted their thermodynamic stability and the resulting band alignment, either a type-I, -II, or -III heterojunction according to the literature. We examined two alignment conditions and two lattice matches between MoS_2 and $MoSe_2$. We found that after contact, the band gap of the interface reduced to ≈0.8 eV, which is comparably lower than MoS_2 and $MoSe_2$ intrinsic band gap. Thermoelectric calculations indicate that the heterojunction has an n-type nature, suitable for applications in electronics and photo-electronics. The numerical modeling by the Landauer approach reveals that the proposed heterojunction can achieve excellent behavior as channel material, providing valuable information to pave the research in new TMD Van der Waals devices and applications.

2. Results and Discussion

2.1. Geometrical Optimization of the Heterojunctions

As a comparison point, the resulting interlayer distance for MoS_2 (d_i) is 0.303 nm and for $MoSe_2$ is 0.313 nm, both in agreement with the reported values of 0.309 nm and 0.32 nm,[4,20] indicating an excellent description of the material by our choice of parameters; the complete parameters are listed in **Table 1**. MoS_2 and $MoSe_2$ optimized surfaces were used to generate two types of heterojunctions considering lattice match and alignment between MoS_2 and $MoSe_2$. We considered the alignment to occur in a zigzag or a chalcogen–chalcogen order, labeled as AB or AA, respectively (**Figure 1**). The lattice match between MoS_2 and $MoSe_2$ is as follows: first, we have MoS_2 used as a substrate to support $MoSe_2$, the latter constrained to the MoS_2 lattice parameters. With this, we had a multilayer $MoSe_2$ over MoS_2 with the two AB and AA alignments, having $(MoS_2/MoSe_2)_{AB}$ and $(MoS_2/MoSe_2)_{AA}$, respectively. For a multi/single-layer situation, we set a single layer of $MoSe_2$ over multilayer MoS_2, also in AB and AA, having $(MoS_2/MoSe_2)_{mAB}$ and $(MoS_2/MoSe_2)_{mAA}$, respectively. Second, we placed multilayer MoS_2 on top of a multilayer $MoSe_2$, where the former is constrained to the $MoSe_2$ lattice parameters. Including the multi/single-layer configurations, labels are $(MoSe_2/MoS_2)_{AB}$, $(MoSe_2/MoS_2)_{AA}$, $(MoSe_2/MoS_2)_{mAB}$, and $(MoSe_2/MoS_2)_{mAA}$, respectively, having in total eight possibilities of $MoS_2/MoSe_2$ assembly.

Due to lattice mismatch occurring between MoS_2 and $MoSe_2$, a tensile or compressive strain is naturally present at the heterojunction and is possible to quantify as a strain index $\varepsilon_1 = x\left(\frac{a_2}{a_1} - 1\right)$, being a_2 the lattice parameter of the material on top and a_1 the lattice parameter of the material at the bottom; x

Table 1. Obtained lattice parameters (a and c), Van der Waals bond distance (d_{vdw}), binding energy (E_b), band gap (E_g), work function (W), dielectric constant ($\varepsilon/\varepsilon_0$), and conduction band alignment (ΔE_c) for all the heterojunction configurations, bulk-like, and single layer (SL) models.

Model	a [nm]	c [nm]	d_{vdw} [nm]	E_b [eV atom^{-1}]	E_g [eV]	W [eV]	$\varepsilon/\varepsilon_0$ [–]	ΔE_c [eV]
$(MoS_2/MoSe_2)_{AB}$	0.319	8.500	0.307	6.48×10^{-3}	0.70	4.423	13.6	–0.217
$(MoS_2/MoSe_2)_{AA}$	0.319	8.500	0.322	1.18×10^{-2}	0.67	4.263	13.6	–0.217
$(MoSe_2/MoS_2)_{AB}$	0.332	8.700	0.315	3.05×10^{-2}	0.02	4.287	14.0	0.217
$(MoSe_2/MoS_2)_{AA}$	0.332	8.700	0.321	3.49×10^{-2}	0	5.032	14.90	0.217
$(MoS_2/MoSe_2)_{mAB}$	0.319	5.500	0.298	-1.05×10^{-2}	0.81	4.737	11.8	–0.217
$(MoS_2/MoSe_2)_{mAA}$	0.319	5.500	0.312	-9.15×10^{-4}	0.76	4.681	11.8	–0.217
$(MoSe_2/MoS_2)_{mAB}$	0.332	5.700	0.279	3.15×10^{-3}	0.085	4.831	12.8	0.217
$(MoSe_2/MoS_2)_{mAA}$	0.332	5.700	0.318	1.03×10^{-2}	0	4.621	14.0	0.217
MoS_2 (bulk-like)	0.319	5.400	0.303[a)]	–	1.66	–	10.2	–
$MoSe_2$ (bulk-like)	0.332	5.550	0.313[a)]	–	1.44	–	11.5	–
MoS_2 (SL)	3.19	–	–	–	2.16	5.503	6.70	–
$MoSe_2$ (SL)	3.32	–	–	–	1.98	4.772	6.55	–

[a)]In this case d_{vdw} is the resulted interlayer distance (d_i) for bulk-like MoS_2 and $MoSe_2$.

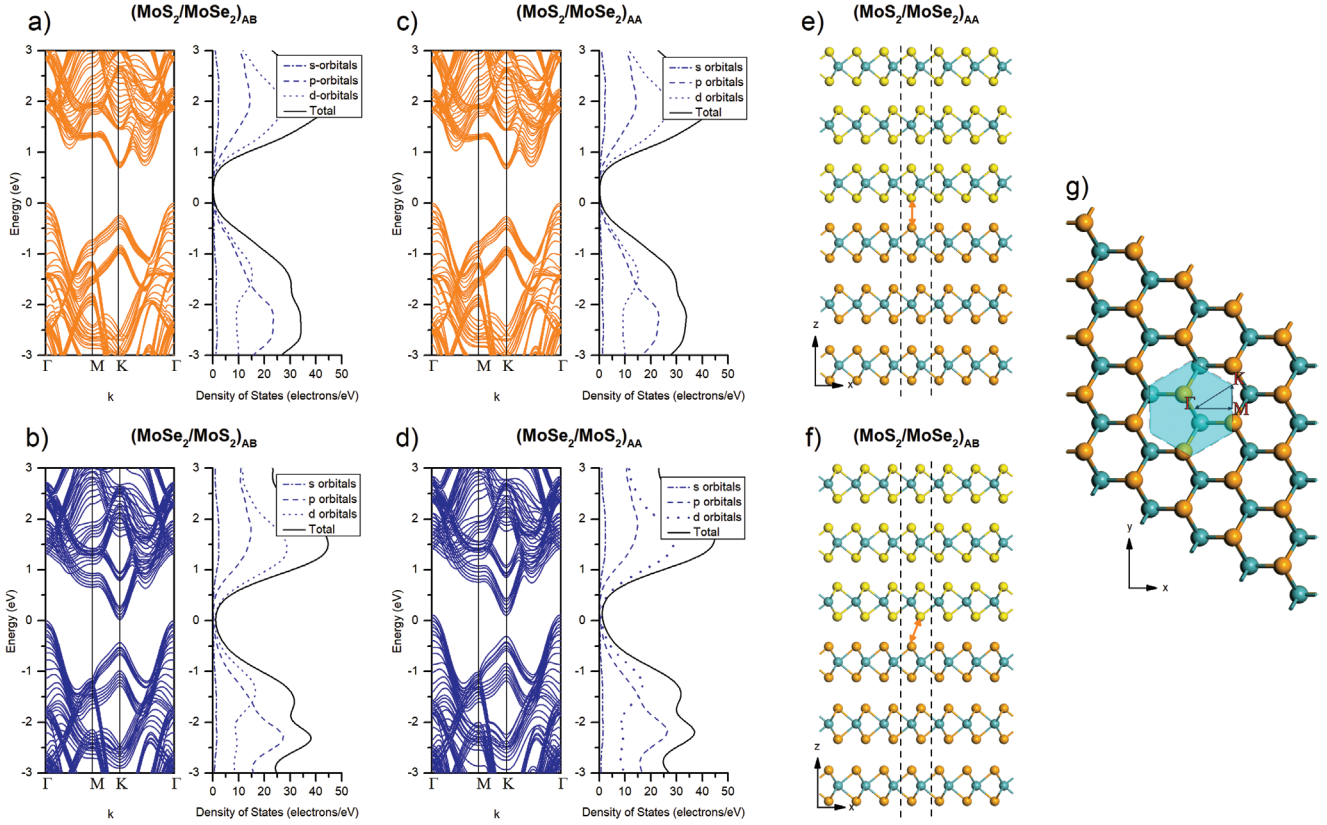

Figure 1. a–d) Resulted band structures and density of states for the multilayer heterojunctions in the AB and AA configuration, e) $(MoS_2/MoSe_2)_{AB}$, and f) $(MoS_2/MoSe_2)_{AA}$ heterojunction models where cyan balls represent molybdenum ions, yellow balls represent sulfur ions and orange selenium ones; the cell is extended in the *z*–*x* plane. Dashed lines in (e) and (f) represent the boundaries of the cell; orange arrows indicate the alignment between chalcogen ions. g) The Brillouin Zone and the Γ-M-K-Γ path used for the band structure calculation and the model extended in the *y*–*x* plane.

is the ratio of layers between material at the bottom and the total number of layers composing the heterojunction. Hence, a compression strain value of –1.96% is present at the $MoSe_2/MoS_2$ heterojunctions, while a tensile strain value of 2.04% is present at $MoS_2/MoSe_2$ configurations. In the multi/single-layer circumstance, a compression strain value of –0.33% and a strain value of 0.34% are present for $MoSe_2/MoS_2$ and $MoS_2/MoSe_2$ models, respectively. In terms of bonding distance between materials, AA alignment leads to larger values of Van der Waals binding distance (d_{vdW}) compared to AB alignments (Table 1); except for the case of $(MoS_2/MoSe_2)_{mAA}$ and $(MoSe_2/MoS_2)_{mAB}$ with the zigzag arrangement, all binding distance values resulted above 0.3 nm (Figure S1, Supporting Information).

The binding energy (E_b) helped to determine the thermodynamic stability of the heterojunction model, and it was computed using the following expression, in units of eV atom^{-1},

$$E_b = \frac{1}{n}\left(E_{ht} - E_{MoS} - E_{MoSe}\right) \quad (1)$$

being E_{ht}, E_{MoS}, E_{MoSe}, and n the total energy of the heterostructure, the total energy of MoS_2 surface, the total energy of $MoSe_2$ surface, and the number of atoms in the structure, respectively. Six of our eight models resulted in endothermic values of E_b, between 6.48×10^{-3} eV atom^{-1} and 1.03×10^{-2} eV atom^{-1} (see also Table 1) with linear trend between multilayer and multi/single-layer arrangements (Figure S2, Supporting Information); these values compare to previous reports on similar heterojunction theoretical models.[27] Endothermic values of binding energy do not necessarily indicate unfavorable or unstable structures. The order of magnitude of this result implies the presence of weak Van der Waals contacts, possibly by electrostatic interactions. This also suggests that energy demand is required to achieve the desired structure interpreted as a degree of control for experimental fabrication of Van der Waals heterostructures; it is possible to supply such an amount of energy by annealing process or photo-induced annealing as reported elsewhere.[28,29]

2.2. Electronic Structure of $MoS_2/MoSe_2$ Heterojunctions

All $MoS_2/MoSe_2$ models, i.e., $MoSe_2$ is constrained to MoS_2 lattice, resulted in higher band gap values than $MoSe_2/MoS_2$ models; similarly, models with AB alignment resulted also with higher band gap values than models with AA alignment (Table 1). $MoSe_2/MoS_2$ heterojunctions resulted in close-to-zero band gap values. This fact cannot be attributed to the exchange–correlation functional because our computations for bulk-like and single layer MoS_2 and $MoSe_2$ are in complete agreement

with similar reports in the literature.[24,25,30] We attribute the reduction of the band gap to d-orbital contributions which are displaced to energy levels just inside the band gap (Figure 1) because of lattice constraint. According to our results, the highest band gap value was achieved by $(MoS_2/MoSe_2)_{mAB}$ heterojunction configuration, being E_g = 0.805 eV (indirect band gap at Γ-K). On the other hand, $(MoSe_2/MoS_2)_{AA}$ and $(MoSe_2/MoS_2)_{mAA}$ models do not present any band gap, while $(MoSe_2/MoS_2)_{AB}$ and $(MoSe_2/MoS_2)_{mAB}$ cases yield a reduced band gap of 0.022 eV and 0.085 eV, respectively (Figure S3, Supporting Information).

We observe that in most $MoSe_2/MoS_2$ heterojunction configurations, the CBM becomes noticeable at the **K** point after the interface formation. This phenomenon causes an intercrossing with the Fermi level and, hence, a semi-metallic character, as reported in bent heterostructures.[11,31,32] In contrast, $MoS_2/MoSe_2$ configuration has lesser metallic d-orbital contribution around the conduction band, translated as a lower disturbance of molybdenum d orbitals by interlayer interactions as previously suggested.[11,33] Also, chalcogen orbitals' distribution, specifically 3p orbitals from sulfur and 4p from selenium, primarily contributing to the valence band, increase more pronounced at the $MoSe_2/MoS_2$ heterojunction, getting dispersed to higher energy values and causing band gap reduction, supporting our premise on lattice constraint and band gap reduction.

2.2.1. Band Offset and Band Alignment Calculation

In this work, we considered the position of the macroscopic average electrostatic potential of both materials, MoS_2 and $MoSe_2$, throughout the interface and used it as a reference point to locate the bulk VBM. With this, we estimated the band alignment in the $MoS_2/MoSe_2$ heterojunction as done in other reports.[34,35] This macroscopic potential generates a potential band offset determined by the difference in the electrostatic potential between the two regions (in the *xy* plane) of the heterojunction denoted as Δ*V* (**Figure 2**). Electrostatic

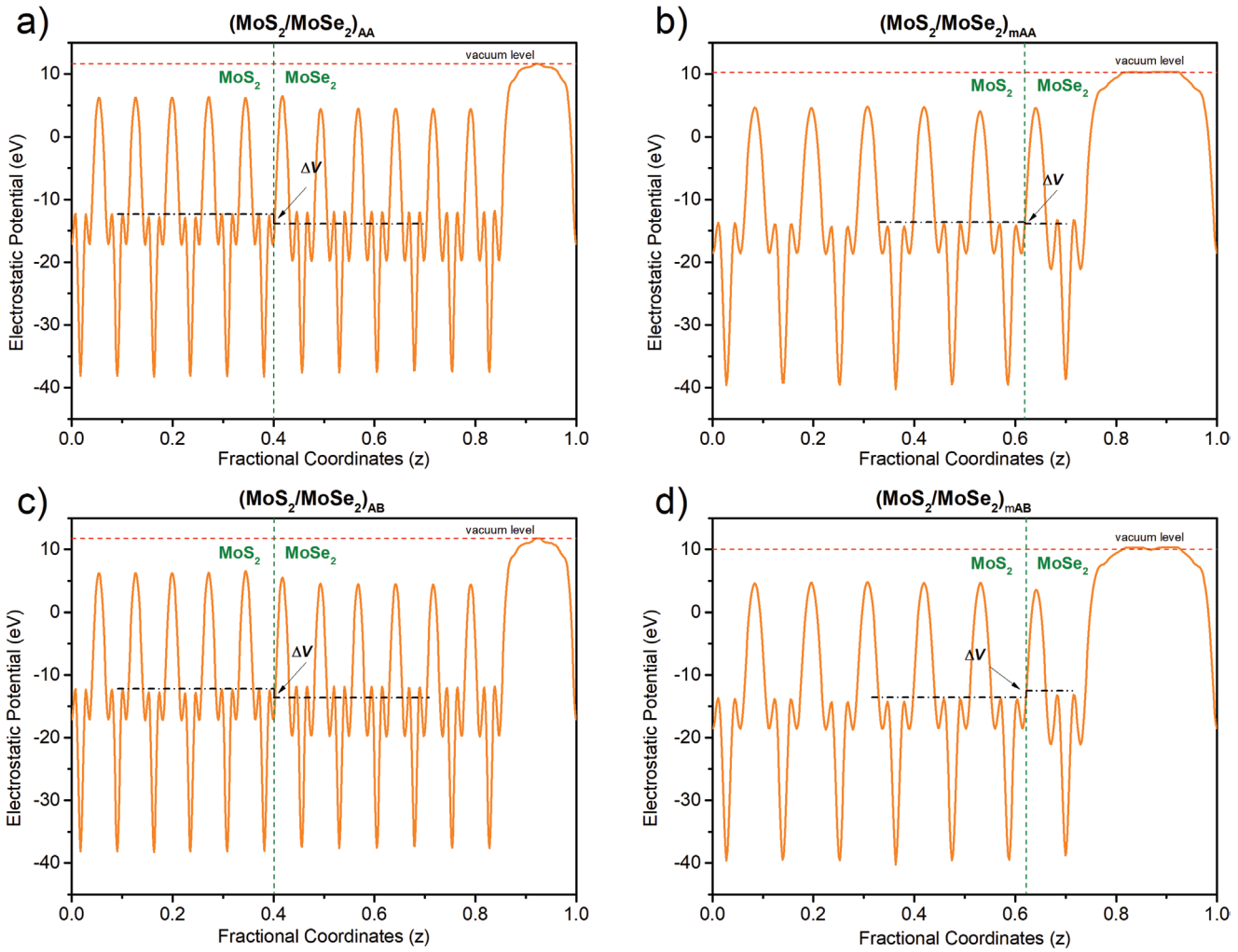

Figure 2. Averaged electrostatic potentials plots (in the *xy* plane) of $MoS_2/MoSe_2$ heterojunction configurations; green line indicates the point at which the interface is located, red line indicates the position of vacuum level. Dashed-dotted lines represent the average electrostatic potential of both materials and Δ*V* is the difference in the electrostatic potential energy.

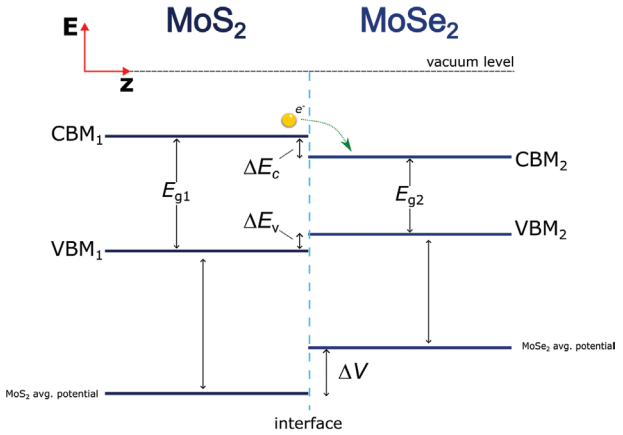

Figure 3. Schematic of band alignment between $MoS_2/MoSe_2$ heterojunction scenarios, where is possible to observe the ΔE_c and ΔE_v, which are the energy difference of conduction and valence bands, respectively.

potential plots for the $MoSe_2/MoS_2$ heterojunction configuration are depicted in Figure S4 (Supporting Information). Then, the valence band offset is computed as

$$\Delta E_V = E_V^{top} - E_V^{bottom} + \Delta V \quad (2)$$

where E_V^{top} and E_V^{bottom} are the location of the valence band maximum of the material atop and at the bottom in each of our proposed heterojunction models concerning the average electrostatic potential. Finally, the conduction band offset is found as

$$\Delta E_C = E_g^{top} - E_g^{bottom} + \Delta E_V \quad (3)$$

where E_g^{top} and E_g^{bottom} are the band gap values of the material placed on top and at the bottom in the heterostructure models. Computation gives $\Delta E_c = -0.217$ eV for $MoS_2/MoSe_2$ heterojunctions, while $\Delta E_c = 0.217$ eV resulted for $MoSe_2/MoS_2$ (Table 1) corresponding to a type-I heterostructure and represented in **Figure 3**. Our results on ΔE_c are comparable to those reported in polar and nonpolar heterostructures using ZnO, GaN, and $MgGeN_2$;[34] Quan et al. estimated experimentally a ΔE_c of 0.46 eV in a $MoTe_2/MoS_2$ nanocomposite film,[36] comparable to our estimation. Thus, this indicates the potential use of $MoS_2/MoSe_2$ heterojunction in electronic devices. In this case, charge carriers (electrons or holes) get confined at the material with the lower band gap due to this band alignment. The effect of charge confinement has been reported in Si/MoS_2 heterostructures,[37] helping to increase charge injection yield. This result could be used as theoretical insights in designing metal-oxide field–effect transistors (MOSFET) and improved solar cells devices using TMD heterojunctions as channel materials.

In $MoSe_2/MoS_2$ heterojunction configurations, theoretically, an inverted version of the band alignment described in Figure 3 should describe the behavior of the bands after contact, but as presented by band structure calculations, a semimetallic nature indicates a much more complicated band alignment, possibly with induced gap states and dipole formation at the interface.

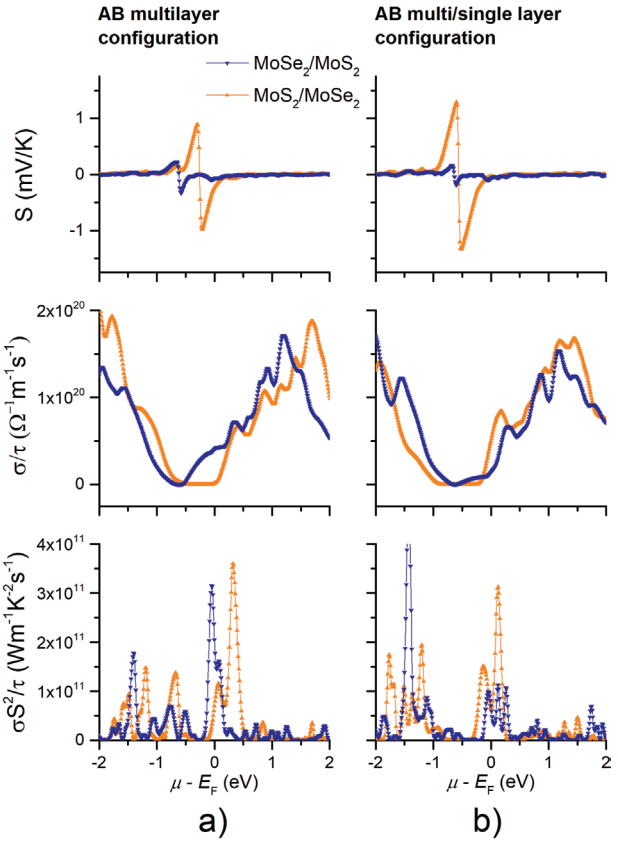

Figure 4. Seebeck coefficient (S), conductivity (σ/τ) and power factor ($S^2\sigma/\tau$) calculation for AB heterojunction configuration at 300 K as function of $\mu - E_0$. Seebeck coefficient values of $MoS_2/MoSe_2$ indicate a semiconductor behavior around the Fermi level. Power factor ($S^2\sigma/\tau$) values are higher at the $MoS_2/MoSe_2$ heterojunctions because of their higher values of Seebeck coefficient.

2.3. Thermoelectric Properties

For further analysis, the Seebeck coefficient (S) allows us to predict the behavior of charge carriers along energy levels near the Fermi level. From our calculations of the Seebeck coefficient, in all heterojunctions the crossover from hole-controlled to electron-controlled conduction, i.e., going from positive to negative values, takes place before $\mu - E_F = 0$ (**Figure 4**), indicating that electron-controlled conduction dominates.[38] Seebeck coefficient is symmetric around the crossover point in $MoS_2/MoSe_2$ heterojunction configurations; however, the $MoSe_2/MoS_2$ configurations are slightly asymmetrical just around the crossover point.

We observe that the Seebeck coefficient in $(MoS_2/MoSe_2)_{mAB}$ heterojunction resulted in ≈1300 μV K^{-1}, the highest value found (Figure 4). By contrast, $(MoSe_2/MoS_2)_{mAB}$ has the lowest Seebeck coefficient of all heterojunction configurations studied, at about 210 μV K^{-1}. Our computed Seebeck coefficient values are consistent with previous experimental measurements on few-layer MoS_2 and MoS_2/WSe_2 heterojunction,[39–41] only being somewhat overestimated, attributed to factors like electron–phonon scattering, recombination processes, and structural defects. In addition, the crossover in $MoSe_2/MoS_2$ heterojunctions takes place at lower energy levels than in $MoS_2/MoSe_2$,

which can be associated with the low band gap and semimetallic behavior observed in the band structure plots.

Calculations on conductivity per relaxation time (σ/τ) show a pronounced n-type character for $MoS_2/MoSe_2$ heterojunctions (Figure 4). In contrast, $MoSe_2/MoS_2$ confirms our previous suggestions where $MoSe_2/MoS_2$ heterojunctions have a semimetallic behavior due to metallic d-orbital reallocation. Thermoelectric properties for heterojunctions in the AA configuration have the same trend as the AB configuration, indicating little dependence on this alignment condition (Figure 4 and Figure S5, Supporting Information). In general, $MoS_2/MoSe_2$ heterojunctions in the multi/single configuration have improved transport properties than the other configurations considered in this work, with higher Seebeck coefficient and values of σ/τ around the band gap in the order of 10^{20}. This behavior follows previous work suggesting that multilayer configurations of MoS_2 have enhanced light adsorption.[42] In terms of the power factor ($S^2\sigma/\tau$), $MoS_2/MoSe_2$ heterojunctions are superior to $MoSe_2/MoS_2$ ones due to higher values of the Seebeck coefficient.

2.4. Heterojunction Model in a One-Gate Configuration

As a further examination, we model our heterojunction as a one-gate device resembling a transistor configuration. For this, we consider the Landauer approach, the ballistic transport regime, and non-degenerate statistics. We computed the current versus drain-to-source voltage (I–V) characteristic using the following expression

$$I_{ds} = wQ_n v_t \left[\frac{1-e^{-qV_{ds}/k_bT}}{1+e^{-qV_{ds}/k_bT}}\right] \quad (4)$$

which is a function of the surface charge (Q_n) that varies with respect to the drain to source voltage (V_{ds}) and gate voltage (V_{gs}). v_t represents the charge thermal velocity in the ballistic regime (and non-degenerate statistics) and w is the width of the device. A more detailed description of this approach is provided in the Supporting Information. We aimed to test the material's capabilities for electronic applications, benefiting from the resulting type-I alignment. The only heterojunctions considered are $(MoS_2/MoSe_2)_{AB}$ and $(MoS_2/MoSe_2)_{mAB}$ based on our previous results on band structure and thermoelectric calculations.

First, the surface charge needed to be computed, denoted by Q_n, for each of the considered heterojunction models. This was by using a semi-empirical expression developed by Wright et al.,[43] which states that

$$Q_n = -mC_g\left(\frac{k_bT}{q}\right)\ln\left(1+e^{q(V_{gs}-V_t)/mk_bT}\right) \quad (5)$$

where m is the body effect parameter (≈1 for thin oxide layers), C_g is the gate capacitance, V_t is the threshold voltage, and k_b is the Boltzmann constant. To evaluate C_g we considered HfO_2 as dielectric material—high dielectric constant of 25—with a thickness (t_{ox}) of 10 nm (see Supporting Information). Similarly, we employed the resulting dielectric constant of 13.6 for the $MoS_2/MoSe_2$ multilayer heterojunction configuration and a dielectric constant of 11.8 for the $MoS_2/MoSe_2$ multi/single-layer heterojunction (Table 1). We extracted these values at the limit where the dielectric function of the heterojunctions approaches zero ($\varepsilon(E) \to 0$). The semiconductor thickness (t_s) was set to 7.2 nm which is approximately the thickness of our heterojunction models.

Second, we input the following parameters and function Q_n into Equation (4) to compute the I–V characteristics of the modeled one-gate device: a thermal velocity $v_t = \sqrt{\frac{2k_BT}{\pi m^*}}$ considering an electron effective mass (m^*) of $MoS_2/MoSe_2$ approximately equal to the effective mass of MoS_2, [20,44] being $0.46m_0$; a width (w) of the one-gate device of 400 nm, and a channel length of 10 nm.[45] Finally, the drain-to-source voltage was set to –100 mV, while the threshold voltage was –10 V, –5 V, and –1 V. We first validate our model by comparing theoretical I–V characteristics utilizing the parameters of devices as reported in the literature. We found an excellent agreement of our I–V approach with experimentally obtained I–V curves (see Figure S5, Supporting Information), and after that, we proceeded with our parameters as mentioned above.

From the resulting I–V relations of our modelled one-gate device (**Figure 5**), we estimated a subthreshold swing (SS) of 60 mV dec^{-1}, field–effect mobility (μ_f) of 160 $cm^2\ V^{-1}\ s^{-1}$, and an on/off ratio of the order of 10^5 using a threshold voltage of –1 V at –100 mV drain-to-source voltage and a $MoS_2/MoSe_2$ heterojunctions in multilayer configuration (Figure 5a). $MoS_2/MoSe_2$ heterojunctions in multilayer configuration output higher current compared to multi/single-layer ones (Figure 5b), which agrees with the calculations of σ/τ presented earlier. The order of magnitude of the output current agrees with experimental data available (see Supporting Information), confirming that our methodology can potentially assist in designing electronic and opto-electronics devices integrating TMD.

3. Conclusions

Our results from DFT allowed us to determine the electronic structure and transport properties of Van der Waals multilayer and multi/single-layer of $MoS_2/MoSe_2$ and $MoSe_2/MoS_2$ heterostructures with a zigzag (AB) and chalcogen–chalcogen (AA) interlayer alignment. After the formation of the interface, the resulting band gap is around 0.8 eV with a band offset of about 0.2 eV. The $MoS_2/MoSe_2$ heterojunction preserves their semiconducting characteristics. However, $MoSe_2/MoS_2$ configurations have semi-metallic behavior. This shift is strongly related to the interlayer coupling due to induced strain and subsequent reallocation of metallic d-orbital and chalcogen orbitals in energy levels inside the band gap. The resulting band alignment of $MoS_2/MoSe_2$ (in AA and AB alignment configurations) indicates a type-I heterojunction, especially useful in designing optoelectronic and electronic devices. Moreover, the heterojunction presents an excellent Seebeck coefficient of ≈1000 μV K^{-1} and conductivity values (σ/τ) around the band gap in the order of 10^{20}. Numerical modeling of our material in a one-gate transistor indicates excellent behavior as channel material with subthreshold swing values of 60 mV dec^{-1} and

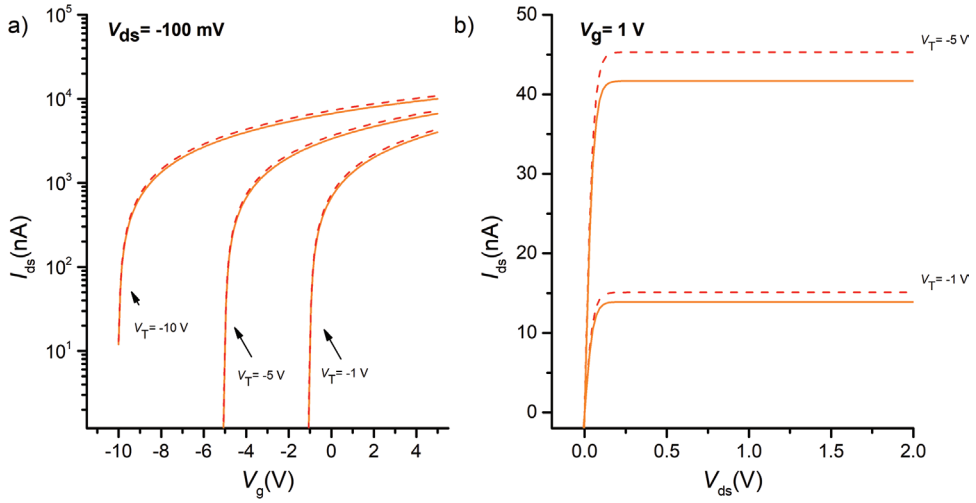

Figure 5. a) Drain-to-source current (I_{ds}) as function of applied gate voltage (V_g) at a constant drain-to-source voltage (V_{ds}) of –100 mV and setting three threshold voltages (V_T): –10, –5, and –1 V. Dashed lines correspond to the calculations using the $MoS_2/MoSe_2$ multilayer heterojunctions configuration with an estimated dielectric constant of 13.6; solid lines correspond to the $MoS_2/MoSe_2$ multi/single-layer heterojunctions with a dielectric constant of 11.8. b) I_{ds} as a function of V_{ds} with $V_g = 1$ V at different values of V_T.

field–effect mobilities of about 160 cm^{-2} V^{-1} s^{-1}. As presented here, these heterojunctions have promising applications in electronic and optoelectronics applications, owing to their remarkable electronic and thermoelectric properties.

4. Experimental Section

Density Functional Calculations: Geometric optimization calculations were completed using DFT code CASTEP[46] employing the revised Perdew—Burke–Herzenhof (RPBE) as the exchange–correlation functional, part of the Generalized Gradient Approximation (GGA). Geometric optimization criteria were set as follows: cutoff energy at 500 eV, a self-consistent field tolerance of 10^{-6} eV $atom^{-1}$, a k-point separation of 0.6 nm^{-1} (0.06 $Å^{-1}$), a maximum displacement of 10^{-4} nm (10^{-3} Å), a convergence tolerance for maximum energy difference of 10^{-5} eV $atom^{-1}$, and a maximum force threshold of 0.3 eV nm^{-1} (3×10^{-2} eV $Å^{-1}$). The ultrasoft pseudopotentials and the semi-empirical DFT-D2 adjustment were employed in all the DFT calculations for long-range dispersion correction as described by Grimme[47] and as used in previous studies for accurate description of layered materials.[20,48–50] For the electronic structure estimation, GGA and Perdew–Burke–Ernzerhof (PBE) were chosen, along with a k-point separation of 0.01 nm^{-1} (0.001 $Å^{-1}$) in the Γ-M-K-Γ path. Thermoelectric properties were calculated using Boltztrap2 code[51] which solves the linearized Boltzmann transport equation. The quasi-particle energies were calculated with WIEN2k code[52] and used as input for Boltztrap2 calculations; details are provided in the Supporting Information.

Molecular Models of $MoS_2/MoSe_2$ Heterojunction: The optimized MoS_2 and $MoSe_2$ unit cells (space group P63/mmc) had lattice parameters of $a = b = 0.319$ nm and $c = 1.27$ nm and $a = b = 0.332$ nm and $c = 1.29$ nm, respectively. Using these models, the MoS_2 and $MoSe_2$ surfaces were constructed in the ⟨002⟩ direction, setting a thickness of ≈2.0 nm for each. This surface model consists of six Mo atoms and twelve chalcogen atoms (either S or Se), and each of these surfaces resembles a bulk-like material. The heterojunction models were assembled as mentioned previously in the text. A vacuum space of ≈1.5 nm in the z direction separates periodic images, avoiding undesired contacts and interactions. These surface and heterojunction models were subjected to geometry optimization using the abovementioned parameters.

Supporting Information

Supporting Information is available from the Wiley Online Library or from the author.

Acknowledgements

This work received support from Instituto de Ingeniería y Tecnología of Universidad Autónoma de Cd. Juárez (UACJ) and Programa de Fortalecimiento a la Calidad Educativa (PFCE) 2016-2017 of Instituto de Ingeniería y Tecnología for licensing BIOVIA-Materials Studio and the use of high-performance computing facilities. Oscar A. López-Galán thanks the support from Consejo Nacional de Ciencia y Tecnología (CONACYT) from México through graduate scholarship program of Programa Nacional de Posgrados de Calidad (PNPC) application number 790769 and the fellowship granted by the KAAD from Germany. The authors thankfully acknowledge the computer resources and support provided by Laboratorio Nacional de Informática (LANTI-UACJ). I.P. is grateful to Oscar Ruiz from LANTI for technical support. Part of this work was a collaboration with the Center for Integrated Nanotechnologies (CINT), an Office of Science User Facility operated for the U.S. Department of Energy (DOE) Office of Science. All authors appreciate the fruitful discussion and suggestions from Torben Boll and Martin Heilmaier from KIT. All authors contribute equally to this work. The authors acknowledge support by the KIT-Publication Fund of the Karlsruhe Institute of Technology.

Open access funding enabled and organized by Projekt DEAL.

Conflict of Interest

The authors declare no conflict of interest.

Data Availability Statement

The data that support the findings of this study are available from the corresponding author upon reasonable request.

Keywords

band gap, density functional theory, heterojunctions, semiconductors

Received: November 8, 2022
Revised: January 30, 2023
Published online:

[1] A. Splendiani, L. Sun, Y. Zhang, T. Li, J. Kim, C.-Y. Chim, G. Galli, F. Wang, *Nano Lett.* **2010**, *10*, 1271.
[2] R. I. Romanov, M. G. Kozodaev, Y. Yu. Lebedinskii, I. V. Zabrosaev, E. A. Guberna, A. M. Markeev, *Phys. Status Solidi A* **2021**, *218*, 2000744.
[3] K. F. Mak, C. Lee, J. Hone, J. Shan, T. F. Heinz, *Phys. Rev. Lett.* **2010**, *105*, 136805.
[4] M. Ramos, J. Nogan, M. Ortíz-Díaz, J. L. Enriquez-Carrejo, C. A. Rodriguez-González, J. Mireles-Jr-Garcia, C. Ornelas, A. Hurtado-Macias, *Surf. Topogr.: Metrol. Prop.* **2017**, *5*, 025003.
[5] N. Li, Q. Wang, C. Shen, Z. Wei, H. Yu, J. Zhao, X. Lu, G. Wang, C. He, L. Xie, J. Zhu, L. Du, R. Yang, D. Shi, G. Zhang, *Nat. Electron.* **2020**, *3*, 711.
[6] S. Ishihara, Y. Hibino, N. Sawamoto, K. Suda, T. Ohashi, K. Matsuura, H. Machida, M. Ishikawa, H. Sudoh, H. Wakabayashi, A. Ogura, *Jpn. J. Appl. Phys.* **2016**, *55*, 04EJ07.
[7] S. G. Martanov, N. K. Zhurbina, M. V. Pugachev, A. I. Duleba, M. A. Akmaev, V. V. Belykh, A. Y. Kuntsevich, *Nanomaterials* **2020**, *10*, 2305.
[8] X. Zhou, N. Zhou, C. Li, H. Song, Q. Zhang, X. Hu, L. Gan, H. Li, J. Lü, J. Luo, J. Xiong, T. Zhai, *2D Mater.* **2017**, *4*, 025048.
[9] C. Huang, S. Wu, A. M. Sanchez, J. J. P. Peters, R. Beanland, J. S. Ross, P. Rivera, W. Yao, D. H. Cobden, X. Xu, *Nat. Mater.* **2014**, *13*, 1096.
[10] A. Hötger, J. Klein, K. Barthelmi, L. Sigl, F. Sigger, W. Männer, S. Gyger, M. Florian, M. Lorke, F. Jahnke, T. Taniguchi, K. Watanabe, K. D. Jöns, U. Wurstbauer, C. Kastl, K. Müller, J. J. Finley, A. W. Holleitner, *Nano Lett.* **2021**, *21*, 1040.
[11] O. A. López-Galán, M. Ramos, *MRS Commun.* **2022**, *12*, 1154.
[12] T. Roy, M. Tosun, M. Hettick, G. H. Ahn, C. Hu, A. Javey, *Appl. Phys. Lett.* **2016**, *108*, 083111.
[13] J. Kang, J. Li, S.-S. Li, J.-B. Xia, L.-W. Wang, *Nano Lett.* **2013**, *13*, 5485.
[14] M. A. Ramos, R. Chianelli, J. L. Enriquez-Carrejo, G. A. Gonzalez, G. Berhault, *Comput. Mater. Sci.* **2014**, *84*, 18.
[15] A. C. Riis-Jensen, S. Manti, K. S. Thygesen, *J. Phys. Chem. C* **2020**, *124*, 9572.
[16] T. Roy, M. Tosun, X. Cao, H. Fang, D.-H. Lien, P. Zhao, Y.-Z. Chen, Y.-L. Chueh, J. Guo, A. Javey, *ACS Nano* **2015**, *9*, 2071.
[17] D. Chiappe, I. Asselberghs, S. Sutar, S. Iacovo, V. Afanas'ev, A. Stesmans, Y. Balaji, L. Peters, M. Heyne, M. Mannarino, W. Vandervorst, S. Sayan, C. Huyghebaert, M. Caymax, M. Heyns, S. De Gendt, I. Radu, A. Thean, *Adv. Mater. Interfaces* **2016**, *3*, 1500635.
[18] J. Xiao, J. Liu, K. Sun, Y. Zhao, Z. Shao, X. Liu, Y. Yuan, Y. Li, H. Xie, F. Song, Y. Gao, H. Huang, *J. Phys. Chem. Lett.* **2019**, *10*, 4203.
[19] M. Xiong, J. Yan, B. Chai, G. Fan, G. Song, *J. Mater. Sci. Technol.* **2020**, *56*, 179.
[20] L. Ji, J. Shi, Z. Y. Zhang, J. Wang, J. Zhang, C. Tao, H. Cao, *J. Chem. Phys.* **2018**, *148*, 014704.
[21] Z. Zheng, Q. Zheng, J. Zhao, *Electron. Struct.* **2019**, *1*, 034001.
[22] M. Z. Bellus, M. Li, S. D. Lane, F. Ceballos, Q. Cui, X. C. Zeng, H. Zhao, *Nanoscale Horiz.* **2017**, *2*, 31.
[23] H. Terrones, F. López-Urías, M. Terrones, *Sci. Rep.* **2013**, *3*, 1549.
[24] P. Johari, V. B. Shenoy, *ACS Nano* **2012**, *6*, 5449.
[25] X. Hu, L. Kou, L. Sun, *Sci. Rep.* **2016**, *6*, 31122.
[26] Y. Lu, S. B. Sinnott, *ACS Appl. Nano Mater.* **2020**, *3*, 384.
[27] M. Sharma, A. Kumar, P. K. Ahluwalia, R. Pandey, *J. Appl. Phys.* **2014**, *116*, 063711.
[28] R. H. Kim, J. Leem, C. Muratore, S. Nam, R. Rao, A. Jawaid, M. Durstock, M. McConney, L. Drummy, R. Rai, A. Voevodin, N. Glavin, *Nanoscale* **2019**, *11*, 13260.
[29] F. Li, F. Gao, M. Xu, X. Liu, X. Zhang, H. Wu, J. Qi, *Adv. Mater. Interfaces* **2018**, *5*, 1800348.
[30] J. Strachan, A. F. Masters, T. Maschmeyer, *ACS Appl. Energy Mater.* **2021**, *4*, 7405.
[31] S. Xiong, G. Cao, *Nanotechnology* **2016**, *27*, 105701.
[32] H. Cui, J. Li, H. Yuan, *RSC Adv.* **2018**, *8*, 19861.
[33] C. Gong, L. Colombo, R. M. Wallace, K. Cho, *Nano Lett.* **2014**, *14*, 1714.
[34] C. Kaewmeechai, Y. Laosiritaworn, A. P. Jaroenjittichai, *Appl. Surf. Sci.* **2020**, *533*, 147503.
[35] L. Weston, H. Tailor, K. Krishnaswamy, L. Bjaalie, C. G. Van de Walle, *Comput. Mater. Sci.* **2018**, *151*, 174.
[36] C. Quan, C. Lu, C. He, X. Xu, Y. Huang, Q. Zhao, X. Xu, *Adv. Mater. Interfaces* **2019**, *6*, 1801733.
[37] A. Molle, A. Lamperti, D. Rotta, M. Fanciulli, E. Cinquanta, C. Grazianetti, *Adv. Mater. Interfaces* **2016**, *3*, 1500619.
[38] M. Zare, *Phys. Rev. B* **2019**, *99*, 235413.
[39] M. Kayyalha, J. Maassen, M. Lundstrom, L. Shi, Y. P. Chen, *J. Appl. Phys.* **2016**, *120*, 134305.
[40] G. Kogo, B. Xiao, S. Danquah, H. Lee, J. Niyogushima, K. Yarbrough, A. Candadai, A. Marconnet, S. K. Pradhan, M. Bahoura, *Sci. Rep.* **2020**, *10*, 1067.
[41] L. C. Rave-Osorio, J. Alvarez-Quintana, *Appl. Phys. Lett.* **2020**, *116*, 243501.
[42] M.-L. Tsai, S.-H. Su, J.-K. Chang, D.-S. Tsai, C.-H. Chen, C.-I. Wu, L.-J. Li, L.-J. Chen, J.-H. He, *ACS Nano* **2014**, *8*, 8317.
[43] G. T. Wright, *Electron. Lett.* **1985**, *21*, 223.
[44] S. Larentis, H. C. P. Movva, B. Fallahazad, K. Kim, A. Behroozi, T. Taniguchi, K. Watanabe, S. K. Banerjee, E. Tutuc, *Phys. Rev. B* **2018**, *97*, 201407.
[45] B. Radisavljevic, A. Radenovic, J. Brivio, V. Giacometti, A. Kis, *Nat. Nanotechnol.* **2011**, *6*, 147.
[46] S. J. Clark, M. D. Segall, C. J. Pickard, P. J. Hasnip, M. I. J. Probert, K. Refson, M. C. Payne, *Z. Kristallog. – Cryst. Mater.* **2005**, *220*, 567.
[47] S. Grimme, *J. Comput. Chem.* **2006**, *27*, 1787.
[48] T. Bučko, J. Hafner, S. Lebègue, J. G. Ángyán, *J. Phys. Chem. A* **2010**, *114*, 11814.
[49] R. N. Somaiya, Y. Sonvane, S. K. Gupta, *Superlattices Microstruct.* **2021**, *152*, 106858.
[50] T. Hussain, D. Singh, S. K. Gupta, A. Karton, Y. Sonvane, R. Ahuja, *Appl. Surf. Sci.* **2019**, *469*, 775.
[51] G. K. H. Madsen, J. Carrete, M. J. Verstraete, *Comput. Phys. Commun.* **2018**, *231*, 140.
[52] P. Blaha, K. Schwarz, F. Tran, R. Laskowski, G. K. H. Madsen, L. D. Marks, *J. Chem. Phys.* **2020**, *152*, 074101.